



OPEN

DATA DESCRIPTOR

A dataset of rodent cerebrovasculature from *in vivo* multiphoton fluorescence microscopy imaging

Charissa Poon^{1,2}✉, Petteri Teikari³, Muhammad Febrian Rachmadi², Henrik Skibbe² & Kullervo Hynynen¹

We present MiniVess, the first annotated dataset of rodent cerebrovasculature, acquired using two-photon fluorescence microscopy. MiniVess consists of 70 3D image volumes with segmented ground truths. Segmentations were created using traditional image processing operations, a U-Net, and manual proofreading. Code for image preprocessing steps and the U-Net are provided. Supervised machine learning methods have been widely used for automated image processing of biomedical images. While much emphasis has been placed on the development of new network architectures and loss functions, there has been an increased emphasis on the need for publicly available annotated, or segmented, datasets. Annotated datasets are necessary during model training and validation. In particular, datasets that are collected from different labs are necessary to test the generalizability of models. We hope this dataset will be helpful in testing the reliability of machine learning tools for analyzing biomedical images.

Background & Summary

Blood vessel segmentation is often a necessary prerequisite for extracting meaningful analyses from biomedical imaging data. By creating a segmentation, or a mask, that separates vascular from non-vascular pixels, structural information about the vascular system can be acquired, such as diameter, branch order, and blood vessel type. Identification of blood vessels as arterioles, venules, or capillaries can be used to analyze vascular dynamics, such as blood flow and vascular supply. Blood vessel segmentation has clear clinical value. For example, in ischemic stroke studies, vascular segmentation enables detection and quantification of vascular occlusions, which can be helpful in determining therapeutic options^{1,2}. Structural characteristics can also be used as predictors or markers to assist in the diagnosis of diseases, such as Alzheimer's disease^{3,4}, traumatic brain injury⁵, brain tumours⁶, atherosclerosis⁷, and retinal pathology^{8,9}.

Apart from vascular analyses, blood vessel segmentation is also a necessary preprocessing step for the analysis of cells and pathological entities (Fig. 1). In addition to the endothelial and mural cells that make up the blood vessel proper, various other cell types interact with vascular walls, including astrocyte endfeet processes, perivascular macrophages, and peripheral leukocytes. Such cells and their interactions with vasculature can be identified and analyzed based on distance metrics to vascular walls, a task which is simplified with accurate vascular segmentation masks. Vascular-cellular interactions have been of particular interest in studies focused on diseases. For example, recruitment of peripheral leukocytes to cerebrovasculature has been observed following traumatic brain injury¹⁰, middle cerebral artery occlusion¹¹, and in Alzheimer's disease¹². Similar distance metrics can be used to analyze pathological entities, such as perivascular A β plaques¹³ and atherosclerotic plaques¹⁴. Thus, segmentation of blood vessels is a necessary preprocessing step that facilitates further vascular and cellular analyses.

In the neurosciences, two-photon fluorescence microscopy (2PFM) is currently the technique of choice for intravital microscopy. While the resolution of 2PFM can be on par with confocal microscopy, the risk of

¹Sunnybrook Research Institute, Physical Sciences Platform, Toronto, M4N 3M5, Canada. ²RIKEN Center for Brain Science, Brain Image Analysis Unit, Wako-shi, 351-0198, Japan. ³High-Dimensional Neurology Group, University College London Queen Square Institute of Neurology, London, WC1N 3BG, United Kingdom. ✉e-mail: charissa.poon@riken.jp

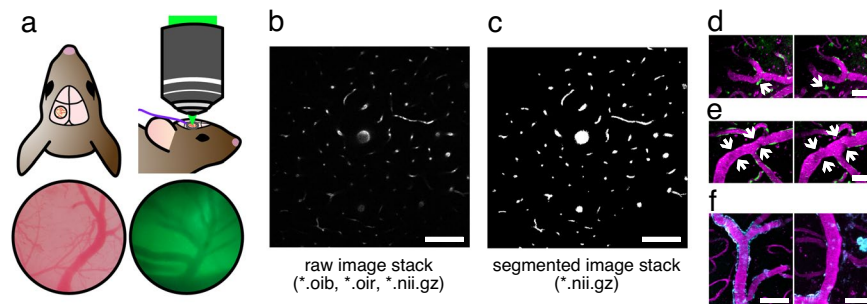


Fig. 1 General workflow for 2PFM image processing. (a) A cranial window was created on the parietal bone, enabling *in vivo* 2PFM imaging. Superficial blood vessels can be observed through the cranial window (left) and ocular lens of the microscope (right). (b) Raw image volumes of rodent cerebrovasculature were collected and saved in Olympus image formats (*.oib, *.oir). (c) Segmentations of blood vessels were achieved using a U-Net and manual corrections. In the MiniVess dataset, raw and segmented image volumes are shared as NIFTI files (*.nii.gz). Segmentation of blood vessels enables downstream analyses, such as (d) cell tracking (arrow), (e) vasoconstriction and dilation (arrows), and (f) analysis of pathological entities, such as A β plaques (cyan). Blood vessels are shown in magenta. Scale bars = 100 μ m in (b,c) and 50 μ m in (d,e,f).

phototoxicity and photobleaching of tissues and fluorophores is substantially reduced because the excitation volume is limited to the focal volume of the microscope¹⁵. The use of longer wavelengths also results in less scattering by the neural tissue, allowing imaging at deeper depths within the brain. 2PFM has been extensively used to investigate various phenomena, including neural activity using voltage-sensitive dyes¹⁶ and calcium indicators¹⁷, microglial activity using transgenic animal models¹⁸, and vascular dynamics¹⁹.

Most methods of automated image processing of 2PFM images rely on proprietary software, such as Imaris (Bitplane, United Kingdom) and Volocity (Quorum Technologies, Canada). Each analysis type, such as vascular segmentation and cell tracking, is generally sold as separate modules. Comprehensive analyses of datasets are therefore functionally limited by the modules available and can become prohibitively expensive. Furthermore, while automated modules produce impressive results for images with high SNR, biomedical images, particularly intravital 2PFM images, are inherently noisy. In practice, substantial manual modifications are required. An open-source alternative is FIJI (Fiji Is Just Image)²⁰. However, FIJI plugins often lack extensive documentation, resulting in a ‘black-box’ nature that may deter and limit use.

Deep learning, such as convolutional neural networks (CNNs) and recent transformer-based model architectures^{21,22}, have been extensively used for automated segmentation tasks in biomedical imaging. For example, the U-Net, a fully CNN, achieves impressive performance in segmenting densely packed neurons in electron microscopy images²³. Clinically, CNNs have achieved state-of-the-art performances in segmenting brain vasculature in magnetic resonance angiography²⁴ and retinal vasculature in optical coherence tomography angiography²⁵ datasets, which have been used to assist in the identification of pathological features.

A common challenge in the application of deep learning models to the biomedical imaging field is the generalizability of models. Models are often exclusively trained on datasets that were collected from a single site. Such models often fail to perform when evaluated on datasets collected at different sites due to a so-called ‘domain shift’ (see e.g. Ouyang *et al.* 2021²⁶ for an example in medical image segmentation), caused by differences in tissue preparation, scanner or microscope set-up, and/or inter-user variability in defining labels^{27,28}. The problem is compounded by poor reporting of the number of evaluation sites and samples used²⁹. One way to improve the reliability and transparency of ML models is to use diverse samples during training, and independent data cohorts for testing³⁰. However, the availability of such annotated, publicly available biomedical imaging datasets is limited due to ethical and privacy concerns, particularly in clinical studies. Another strategy is to use synthetic datasets or publicly available non-biomedical datasets (e.g. ImageNet) as part of the training process, and then evaluate the trained model on the real dataset, a process known as ‘transfer learning’^{31,32}. For example, using transfer learning, a CNN that was pre-trained on a synthetic dataset of blood vessels resulted in impressive segmentation of real mouse brain vasculature³³. However, the availability of real, annotated, field-specific datasets remains to be a need for evaluating the generalizability of models in the biomedical imaging field. In addition, there has been a recent shift in focus from adjusting model parameters to achieve better performance metrics (‘model-centric’), to improving the quality of datasets to improve performance metrics (‘data-centric’), highlighting the importance of high-quality, publicly available datasets.

Public microscopy datasets have been curated by various research groups world-wide. For example, the Human Protein Atlas shows the distribution and expression of proteins and genes across major organ systems^{34–36}, the Broad Bioimage Benchmark Collection contains annotated cell datasets³⁷, and the Allen Brain Cell Types Atlas offers electrophysiological, morphological, and transcriptomic data measured from human and mouse brain. However, vascular datasets have not been as extensively documented. The availability of an annotated 2PFM vascular dataset would assist in diversifying the samples used for training a segmentation model, or in evaluating the performance of segmentation models that were trained on other datasets.

We hereby present MiniVess³⁸, an expert-annotated dataset of 70 3D 2PFM image volumes of rodent cerebrovasculature. The dataset can be used for training segmentation networks^{39,40}, fine-tuning pre-trained networks^{31,32,41}, and as an external validation set for assessing a model’s generalizability⁴². The 3D volumes in this

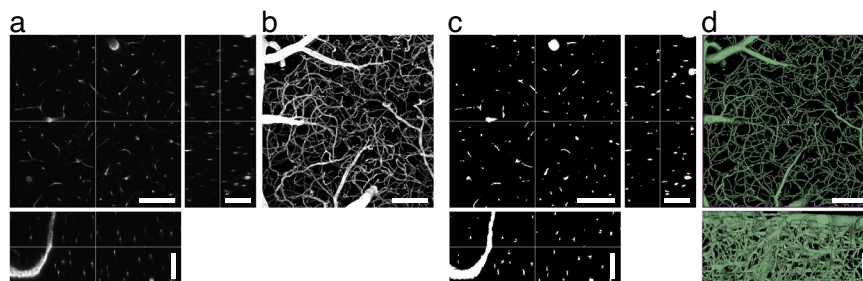


Fig. 2 Example of a raw and segmented image volume pair in the MiniVess dataset. Orthogonal views and maximum projections of (a,b) raw and (c) segmented image volumes. (d) 3D visualization of the whole image volume in (X,Y) and (X,Z) views using 3D Slicer. Scale bars = 100 μ m.

dataset have been curated to only contain clean XYZ imaging in order to ensure correct and consistent annotations, or segmentations, which has been observed to be integral to the evaluation of machine learning models⁴³. Code for image preprocessing and the U-Net workflow are also provided in the MiniVess project Github page. The U-Net code was written using MONAI, a PyTorch-based framework that was built to encourage best practices for AI development in healthcare research. We hope that the availability of the image volumes and code will assist in evaluating the reliability of models built for the analysis of biomedical images.

Methods

Animal preparation. This dataset consists of 2PFM images of the cortical vasculature in adult male and female mice from the C57BL/6 and CD1 strains (20–30 g), and EGFP Wistar rats (Wistar-TgN(CAG-GFP)184ys) (310–630 g)⁴⁴. All animal procedures were approved and conducted in compliance with the Animal Care Committee guidelines at Sunnybrook Research Institute, Canada.

To allow optical access to the brain, an acute cranial window was created over the parietal bone (Fig. 1). Detailed protocols on cranial window procedures have been published elsewhere⁴⁵. Briefly, animals were anesthetized using 1.5–2% isoflurane in a mix of medical air and oxygen. Following fur and scalp removal, a 3–4 mm circle (mice) or rectangle (rats) of bone was removed from the parietal bone using a dental drill, and replaced with a glass cover slip. Due to the thickness of the skull in rats, 1% agarose was deposited onto the brain to prevent air bubbles beneath the cover slip. Animal physiology was monitored using a pulse oximeter, and temperature was maintained using a heating pad with a rectal thermistor. To visualize vasculature, Texas Red 70 kDa dextran (dissolved in PBS, 5 mg/kg; Invitrogen, Canada) was injected through a tail vein catheter. Animals were sacrificed under deep anesthesia using cervical dislocation (mice) or ethanol injection (rats) following the end of imaging.

Imaging. Imaging was conducted using a FV1000MPE multiphoton laser scanning microscope (Olympus Corp., Japan) with an InSight DS tunable laser (Spectra-Physics, USA), or a Ti:Sa laser (MaiTai, Spectra-Physics, Germany). A 25 \times water-immersion objective lens (XLPN25XWMP2, NA 1.05, WD 2 mm, Olympus Corp., Japan) was used to collect 512 \times 512 images with a lateral resolution of 0.621–0.994 μ m/pixel, an imaging speed of 2–8 μ s/pixel, and a step-size of 1–10 μ m, for a maximum depth of 700 μ m. Excitation wavelengths of 810 or 900 nm were used. Fluorescent emissions were collected with photo-multiplier tubes preceded by a 575–645 nm bandpass filter. Images were saved in Olympus's 12-bit .oib or .oir file formats. Acquisition settings were set to utilize the full 12-bit dynamic range (intensity values of 0–4095). Image details are listed in Supplementary Table 1.

File conversions. Image volumes were converted to the NifTI (.nii) file format to make segmentation model prototyping faster, as it is commonly used in neuroimaging and ML frameworks, such as the Medical Open Network for Artificial Intelligence (MONAI, <https://monai.io/>). In MONAI, users can create dataloaders that are customized for their data formats by using Python libraries [such as `tifffile` (available in PyPI), `python-bioformats` (available in PyPI), and `pyometiff` (<https://github.com/filippocastelli/pyometiff>)]. In the future, we plan to develop a dataloader to allow direct use of microscopy formats, skipping the NifTI conversion. Here, we provide the code to convert Olympus files (.oib and .oir) to NifTI (.nii) format, with metadata encoded in the NifTI1 header format. NifTI files were further compressed as .gz archive files (.nii.gz). The original Olympus files are 12-bit, and the exported NifTI files are saved as 16-bit images, as a 12-bit data type is not available. The code also provides options to export each channel separately in multichannel image volumes, separate time volumes as single volumes, and remove top and bottom slices. Further details can be found in the GitHub repository <https://github.com/ctpn/minivess>.

Ground-truth annotation. *Pre-processing.* To create segmented image volumes, images were first pre-processed in Python. Single channel image volumes were individually processed using histogram equalization (to adjust image contrast; scikit-image Contrast Limited Adaptive Histogram Equalization), median filtering (for smoothing; window size = 3, 5), morphological operators (binary closing, to fill holes), and thresholded into binary images. If present, image slices with poor SNR were removed from the top of a stack. Such slices were present if pial vessels were broken during surgery, causing dye to leak on the surface of the brain. *Fine-tuning of*

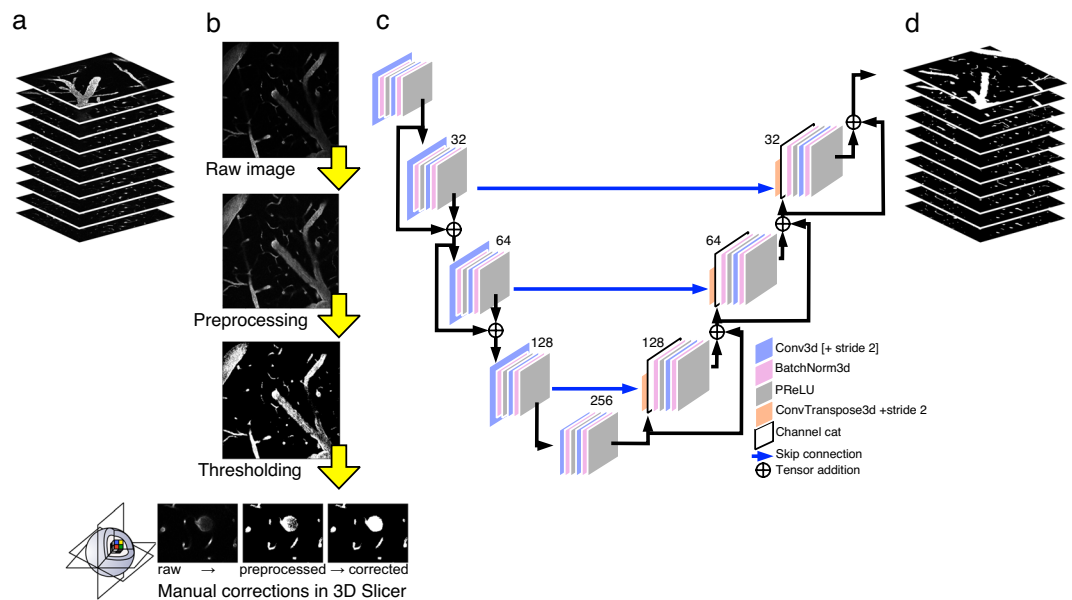


Fig. 3 Blood vessel segmentation workflow. (a) Raw image volumes from 2PFM imaging went through a series of (b) preprocessing steps, followed by manual corrections conducted in 3D Slicer⁴⁶. (c) These segmented image volumes were further refined by using a 2D U-Net, which outputs (d) segmented image volumes. Raw and segmented image volumes, and code for preprocessing and U-Net workflows are provided.

binary images was achieved using the *Paint, Erase, Smoothing, Islands, and Logical operators* effects in the *Segment Editor* module in 3D Slicer⁴⁶. 3D Slicer is a free and open-source platform used for 3D image visualization, segmentation, and registration, among others. For manual corrections, emphasis was placed on minimizing manual drawing to reduce human error, and smoothing edges. For example, jagged borders (arrows) observed in the first round of segmentation are smooth by the final segmentation. A general workflow of the pipeline to achieve ground-truth annotations is shown in Fig. 3. Example image pre-processing code is available in the MiniVess Github repository <https://github.com/ctpn/minivess>.

Machine learning. To improve segmentations, a 2D U-Net²³ was trained using raw images and the preprocessed, segmented images. The U-Net consisted of 5 channels, consisting of 16, 32, 64, 128, and 256 filters, a stride of 2, batch normalization, Adam optimization (1e-4 learning rate), and the Dice loss function. The training was split into 80% for training, 10% for validation, and 10% for testing. Outputs from the U-Net were refined through manual corrections in 3D Slicer, using the same ‘Effects’ listed above. Manual corrections were kept to a minimum to ensure consistency in labels within each volume, and mainly consisted of removing false positives (e.g. noise) and conserving smooth boundaries. Final segmented volumes are the result of five rounds of 2D U-Net and manual corrections in 3D Slicer (Fig. 5). Supervised learning was implemented using the PyTorch-based MONAI framework⁴⁷. MONAI offers open-source, standardized model architectures, data-loaders, and various preprocessing functions that are designed for biomedical imaging. We chose to build use MONAI so that our code can be repurposed to meet other users’ needs. Of note, since the goal was to create a dataset, not a segmentation model, the model used was quite simple.

Data Records

The data is stored in the EBRAINS repository in compressed NiFTi format (*.nii.gz)³⁸. Each raw image stack has an annotated equivalent, designated by a ‘y’ in the file name. Details for each image can be found in the metadata, encoded in the NiFTI1 header format. Each image stack represents a different field-of-view in the cerebrovasculature. Information specific to each image stack can be found in Supplementary Table 1. Maximum projection images of all image volumes are shown in Fig. 4.

Technical Validation

Image volumes were collected and curated by CP (7 years of experience). Ground truth annotations were achieved by using classic image processing tools (see Methods), manual annotations by CP, and a 2D U-Net²³. Accuracy of the final annotations were qualitatively confirmed by CP, and then independently confirmed by MFR and HS (Fig. 2) using 3D Slicer. Final segmentations are the result of 5 rounds of manual annotations or corrections and outputs of the U-Net. A comparison between rounds of segmentations can be found in Fig. 5. Quantitatively, the final round of segmentations showed better agreement and less variation with the fourth round of segmentations, than the first round of segmentations (Table 1).

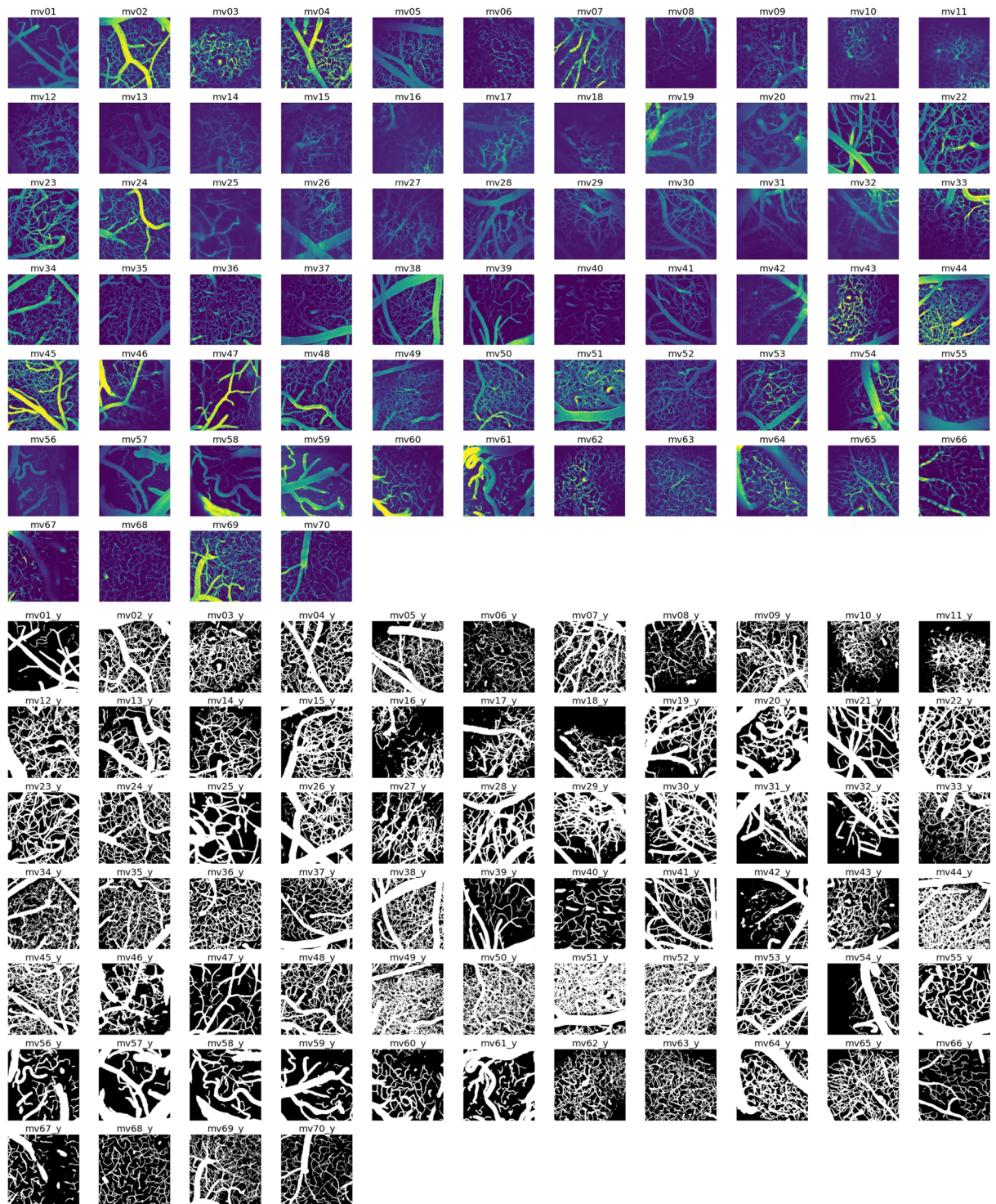


Fig. 4 MiniVess volumes. Maximum projection images of all raw and segmented ('y') image volumes of the MiniVess data are shown for navigation purposes. For clarity, maximum projection images consist of a maximum of 30 slices in each volume. Dark regions within the image volume that appear to have no blood vessels (e.g. diagonal in *mv16*, top of *mv18*) likely have blood vessels, but are difficult to see due to 'shadows' cast by larger blood vessels above, which are not included in the image volume.

Usage Notes

The MiniVess dataset³⁸ contains image volumes of cerebrovasculature from wild-type mouse, transgenic mouse, and transgenic rat brains. Although small in size, the variety of background strains and species in the MiniVess dataset represents rodent strains that are commonly used in wet labs.

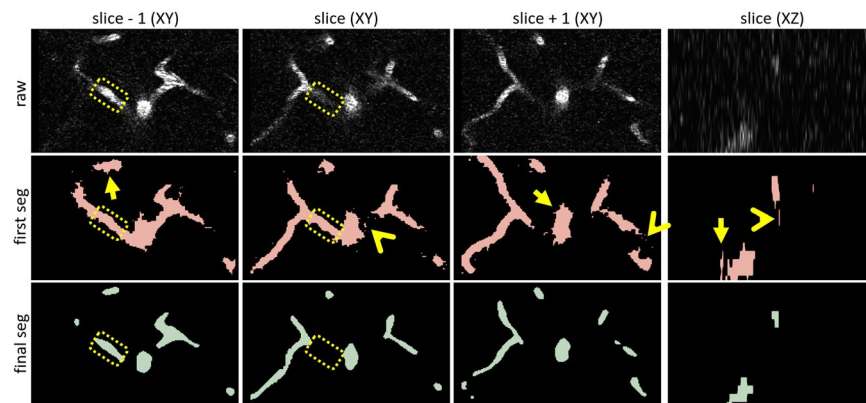


Fig. 5 Validation of segmentations. Cropped images from the XY and XZ planes taken from the raw volume ('raw'), and the first ('first seg') and final ('final seg') rounds of segmentations, are shown for comparison (image volume *mv18*). In addition to the slice-of-interest ('slice (XY)' and 'slice (XZ)'), the image slices above ('slice - 1 (XY)') and below ('slice + 1 (XY)') are also shown. In the first segmentation, vessel edges are less uniform (arrows), spurious noise is evident in the segmentations (angles), and vessel segments that are outside of the slice-of-interest, but present in the slices above or below, are included in the segmentation of the current slice (compare dotted outlines). In contrast, in the final segmentation, vessel edges are more uniform, and segmentations are closer to what is visible in the current slice only, according to acquisition parameters. Each round of segmentation consisted of manual corrections and U-Net outputs. For manual corrections of U-Net outputs, emphasis was placed on minimizing manual drawing to reduce human error, and smoothing edges. For example, jagged borders (arrows) observed in the first round of segmentation are smooth by the final segmentation.

| | Dice (mean) | Dice (SD) |
|---|-------------|-----------|
| first segmentation vs final segmentation | 0.8209 | 0.1202 |
| fourth segmentation vs final segmentation | 0.9913 | 0.0821 |

Table 1. Quantification of the final round of segmentations with the first round, and the fourth round.

The dataset can be downloaded as NiFTi (.nii.gz) files which can then be easily uploaded into machine learning models, or manipulated using FIJI (Fiji Is Just ImageJ), Python, MATLAB, etc. We provide a tutorial of how to use the MiniVess dataset in a U-Net, built in the MONAI framework (<https://github.com/project-monai/monai>). The MONAI framework also provides several tutorials using NiFTi images, which can be further explored using the MiniVess dataset.

Limitations of the dataset. A limitation of the MiniVess dataset is the lack of diversity. All images were collected using the same microscope and lens, by the same operator. Only the species (mouse or rat), sex, and genotype (wild type or non-transgenic TgCRND8⁴⁸) (see EBRAINS metadata³⁸). As such, image quality of the raw image stacks will likely differ from aged or disease animal models that have greater tissue autofluorescence, such as transgenic TgCRND8 mice that exhibit human β -amyloid 40 and β -amyloid 41 (non-transgenic animals do not exhibit pathology⁴⁸).

By making the raw and annotated data available, we hope that the MiniVess dataset can be used as a validation dataset by those evaluating their supervised, semi-supervised, or unsupervised segmentation models, and assist the field to use more data-centric ways to design and evaluate their segmentation models.

Code availability

We provide the Python code to separate multichannel and time series 2PFM image volumes into single volumes, which are easier to manipulate. Multichannel XY, XYZ, XYT, and XYZT images are supported. For multichannel images, the user will be asked to select the channel of interest to export. For images with multi-T volumes (XYT and XYZT), the user has the option of exporting each T-stack separately, or as a single file. We also provide sample code for the image pre-processing tools described above. All code can be accessed at the MiniVess Github repository <https://github.com/ctpn/minivess>.

Received: 13 September 2022; Accepted: 2 March 2023;

Published online: 17 March 2023

References

- Meijs, M. *et al.* Robust segmentation of the full cerebral vasculature in 4D CT of suspected stroke patients. *Sci. Rep.* **7**, 15622, <https://doi.org/10.1038/s41598-017-15617-w> (2017).
- Deshpande, A. *et al.* Automatic segmentation, feature extraction and comparison of healthy and stroke cerebral vasculature. *NeuroImage Clin.* **30**, 102573, <https://doi.org/10.1016/j.nicl.2021.102573> (2021).
- Bennett, R. E. *et al.* Tau induces blood vessel abnormalities and angiogenesis-related gene expression in P301L transgenic mice and human Alzheimer's disease. *Proceedings of the National Academy of Sciences* **115**, E1289–E1298, <https://doi.org/10.1073/pnas.1710329115> (2018).
- Shi, H. *et al.* Retinal vasculopathy in Alzheimer's disease. *Frontiers in Neuroscience* **15**, 1211, <https://doi.org/10.3389/fnins.2021.731614> (2021).
- Park, E., Bell, J. D., Siddiq, I. P. & Baker, A. J. An analysis of regional microvascular loss and recovery following two grades of fluid percussion trauma: A role for hypoxia-inducible factors in traumatic brain injury. *Journal of Cerebral Blood Flow & Metabolism* **29**, 575–584, <https://doi.org/10.1038/jcbfm.2008.151> (2009).
- Jain, R. K. *et al.* Angiogenesis in brain tumours. *Nature Reviews Neuroscience* **8**, 610–622, <https://doi.org/10.1038/nrn2175> (2007).
- Kim, B. J. *et al.* Vascular tortuosity may be related to intracranial artery atherosclerosis. *International Journal of Stroke* **10**, 1081–1086, <https://doi.org/10.1111/ijss.12525> (2015).
- Lains, I. *et al.* Retinal applications of swept source optical coherence tomography and optical coherence tomography angiography. *Progress in Retinal and Eye Research* **84**, 100951, <https://doi.org/10.1016/j.preteyeres.2021.100951> (2021).
- DeBuc, D. C., Rege, A. & Smiddy, W. E. Use of XyCAM RI for noninvasive visualization and analysis of retinal blood flow dynamics during clinical investigations. *Expert Review of Medical Devices* **18**, 225–237, <https://doi.org/10.1080/17434440.2021.1892486> (2021).
- Schwarzmaier, S. M. *et al.* *In vivo* temporal and spatial profile of leukocyte adhesion and migration after experimental traumatic brain injury in mice. *Journal of Neuroinflammation* **10**, 808, <https://doi.org/10.1186/1742-2094-10-32> (2013).
- Desilles Jean-Philippe *et al.* Downstream microvascular thrombosis in cortical venules is an early response to proximal cerebral arterial occlusion. *Journal of the American Heart Association* **7**, e007804, <https://doi.org/10.1161/JAHA.117.007804> (2018).
- Farkas, E. & Luiten, P. G. M. Cerebral microvascular pathology in aging and Alzheimer's disease. *Progress in Neurobiology* **64**, 575–611, [https://doi.org/10.1016/S0301-0082\(00\)00068-X](https://doi.org/10.1016/S0301-0082(00)00068-X) (2001).
- Koronyo, Y. *et al.* Retinal amyloid pathology and proof-of-concept imaging trial in Alzheimer's disease. *JCI Insight* **2**, <https://doi.org/10.1172/jci.insight.93621> (2017).
- Becher, T. *et al.* Three-dimensional imaging provides detailed atherosclerotic plaque morphology reveals angiogenesis after carotid artery ligation. *Circulation Research* **126**, 619–632, <https://doi.org/10.1161/CIRCRESAHA.119.315804> (2020).
- Denk, W., Strickler, J. H. & Webb, W. W. Two-photon laser scanning fluorescence microscopy. *Science* **248**, 73–76, <https://doi.org/10.1126/science.2321027> (1990).
- Kuhn, B., Denk, W. & Bruno, R. M. *In vivo* two-photon voltage-sensitive dye imaging reveals top-down control of cortical layers 1 and 2 during wakefulness. *Proceedings of the National Academy of Sciences* **105**, 7588–7593, <https://doi.org/10.1073/pnas.0802462105> (2008).
- Stosiek, C., Garaschuk, O., Holthoff, K. & Konnerth, A. *In vivo* two-photon calcium imaging of neuronal networks. *Proceedings of the National Academy of Sciences* **100**, 7319–7324, <https://doi.org/10.1073/pnas.1232232100> (2003).
- Szalay, G. *et al.* Microglia protect against brain injury and their selective elimination dysregulates neuronal network activity after stroke. *Nature Communications* **7**, 11499, <https://doi.org/10.1038/ncomms11499> (2016).
- Cruz Hernández, J. C. *et al.* Neutrophil adhesion in brain capillaries reduces cortical blood flow and impairs memory function in Alzheimer's disease mouse models. *Nature neuroscience* **22**, 413–420, <https://doi.org/10.1038/s41593-018-0329-4> (2019).
- Schindelin, J. *et al.* Fiji: An open-source platform for biological-image analysis. *Nature Methods* **9**, 676–682, <https://doi.org/10.1038/nmeth.2019> (2012).
- Hatamizadeh, A., Yang, D., Roth, H. & Xu, D. UNETR: Transformers for 3D medical image segmentation. *arXiv:2103.10504 [cs, eess]* (2021).
- Chen, J. *et al.* TransUNet: Transformers make strong encoders for medical image segmentation. *arXiv:2102.04306 [cs]* (2021).
- Ronneberger, O., Fischer, P. & Brox, T. U-Net: Convolutional networks for biomedical image segmentation. *arXiv:1505.04597 [cs]* (2015).
- Hilbert, A. *et al.* BRAVE-NET: Fully automated arterial brain vessel segmentation in patients with cerebrovascular disease. *Frontiers in Artificial Intelligence* **3**, <https://doi.org/10.3389/frai.2020.552258> (2020).
- Hormel, T. T. *et al.* Artificial intelligence in OCT angiography. *Progress in Retinal and Eye Research* **85**, 100965, <https://doi.org/10.1016/j.preteyeres.2021.100965> (2021).
- Ouyang, C. *et al.* Causality-inspired single-source domain generalization for medical image segmentation. *arXiv:2111.12525 [cs]* (2021).
- Aubreville, M. *et al.* A completely annotated whole slide image dataset of canine breast cancer to aid human breast cancer research. *Scientific Data* **7**, 417, <https://doi.org/10.1038/s41597-020-00756-z> (2020).
- Bertram, C. A. *et al.* Are pathologist-defined labels reproducible? Comparison of the TUPAC16 mitotic figure dataset with an alternative set of labels. In *Interpretable and Annotation-Efficient Learning for Medical Image Computing*, 204–213, https://doi.org/10.1007/978-3-030-61166-8_22 (Springer International Publishing, 2020).
- Wu, E. *et al.* How medical AI devices are evaluated: Limitations and recommendations from an analysis of FDA approvals. *Nature Medicine* **27**, 582–584, <https://doi.org/10.1038/s41591-021-01312-x> (2021).
- Balagurunathan, Y., Mitchell, R. & El Naqa, I. Requirements and reliability of AI in the medical context. *Physica Medica* **83**, 72–78, <https://doi.org/10.1016/j.ejmp.2021.02.024> (2021).
- Zoph, B. *et al.* Rethinking pre-training and self-training. *arXiv:2006.06882 [cs, stat]* (2020).
- Azizi, S. *et al.* Big self-supervised models advance medical image classification. *arXiv:2101.05224 [cs, eess]* (2021).
- Todorov, M. I. *et al.* Machine learning analysis of whole mouse brain vasculature. *Nature Methods* **17**, 442–449, <https://doi.org/10.1038/s41592-020-0792-1> (2020).
- Uhlén, M. *et al.* Tissue-based map of the human proteome. *Science* **347**, <https://doi.org/10.1126/science.1260419> (2015).
- Thul, P. J. *et al.* A subcellular map of the human proteome. *Science* **356**, <https://doi.org/10.1126/science.aal3321> (2017).
- Uhlén, M. *et al.* A pathology atlas of the human cancer transcriptome. *Science* **357**, <https://doi.org/10.1126/science.aan2507> (2017).
- Ljosa, V., Sokolnicki, K. L. & Carpenter, A. E. Annotated high-throughput microscopy image sets for validation. *Nature Methods* **9**, 637–637, <https://doi.org/10.1038/nmeth.2083> (2012).
- Poon, C., Teikari, P., Rachmadi, M. F., Skibbe, H. & Hynynen, K. MiniVess: A dataset of rodent cerebrovasculature from *in vivo* multiphoton fluorescence microscopy imaging (v1). *EBRAINS* <https://doi.org/10.25493/HPBE-YHK> (2022).
- Teikari, P., Santos, M., Poon, C. & Hynynen, K. Deep learning convolutional networks for multiphoton microscopy vasculature segmentation. *arXiv:1606.02382 [cs]* (2016).
- Haft-Javaherian, M. *et al.* Deep convolutional neural networks for segmenting 3D *in vivo* multiphoton images of vasculature in Alzheimer disease mouse models. *PLoS One* **14**, e0213539, <https://doi.org/10.1371/journal.pone.0213539> (2019).
- Reed, C. J. *et al.* Self-supervised pretraining improves self-supervised pretraining. *arXiv:2103.12718 [cs]* (2021).

42. Sanner, A., Gonzalez, C. & Mukhopadhyay, A. How reliable are out-of-distribution generalization methods for medical image segmentation? *arXiv:2109.01668 [cs, eess]* (2021).
43. Northcutt, C. G., Athalye, A. & Mueller, J. Pervasive label errors in test sets destabilize machine learning benchmarks. *arXiv:2103.14749 [cs, stat]* (2021).
44. Hakamata, Y. *et al.* Green fluorescent protein-transgenic rat: A tool for organ transplantation research. *Biochemical and Biophysical Research Communications* **286**, 779–785, <https://doi.org/10.1006/bbrc.2001.5452> (2001).
45. Holtmaat, A. *et al.* Long-term, high-resolution imaging in the mouse neocortex through a chronic cranial window. *Nat. Protoc.* **4**, 1128–1144, <https://doi.org/10.1038/nprot.2009.89> (2009).
46. Fedorov, A. *et al.* 3D Slicer as an image computing platform for the quantitative imaging network. *Magn. Reson. Imaging* **30**, 1323–1341, <https://doi.org/10.1016/j.mri.2012.05.001> (2012).
47. MONAI Consortium. MONAI: Medical open network for AI. *Zenodo* <https://doi.org/10.5281/zenodo.4323058> (2020).
48. Chishti, M. *et al.* Early-onset amyloid deposition and cognitive deficits in transgenic mice expressing a double mutant form of amyloid precursor protein 695. *Journal of Biological Chemistry* **276**, 21562–21570, <https://doi.org/10.1074/jbc.m100710200> (2001).

Acknowledgements

This work was supported by funding from the National Institute of Biomedical Imaging and Bioengineering of the National Institutes of Health (RO1-EB003268, awarded to K.H.), the Canadian Institutes of Health Research (FDN 154272, awarded to K.H.), and the Temerty Chair in Focused Ultrasound Research at Sunnybrook Health Sciences Centre. This work was also supported by the program for Brain Mapping by Integrated Neurotechnologies for Disease Studies (Brain/MINDS) from the Japan Agency for Medical Research and Development AMED (JP15dm0207001).

Author contributions

C.P. and P.T. contributed equally to this work. P.T. conceived the experiment. C.P. and P.T. wrote code for data conversion and the U-Net. C.P. conducted the experiments and analyzed the results. C.P. and P.T. wrote the manuscript. All authors reviewed the manuscript.

Competing interests

The authors declare no competing interests.

Additional information

Supplementary information The online version contains supplementary material available at <https://doi.org/10.1038/s41597-023-02048-8>.

Correspondence and requests for materials should be addressed to C.P.

Reprints and permissions information is available at www.nature.com/reprints.

Publisher's note Springer Nature remains neutral with regard to jurisdictional claims in published maps and institutional affiliations.



Open Access This article is licensed under a Creative Commons Attribution 4.0 International License, which permits use, sharing, adaptation, distribution and reproduction in any medium or format, as long as you give appropriate credit to the original author(s) and the source, provide a link to the Creative Commons license, and indicate if changes were made. The images or other third party material in this article are included in the article's Creative Commons license, unless indicated otherwise in a credit line to the material. If material is not included in the article's Creative Commons license and your intended use is not permitted by statutory regulation or exceeds the permitted use, you will need to obtain permission directly from the copyright holder. To view a copy of this license, visit <http://creativecommons.org/licenses/by/4.0/>.

© The Author(s) 2023